Diplexer-Based Fully Passive Harmonic Transponder for Sub-6-GHz 5G-Compatible IoT Applications

Xiaoqiang Gu, Nikhil Srinaga, Lei Guo, Simon Hemour, Ke Wu

Diplexer-Based Fully Passive Harmonic Transponder for Sub-6-GHz 5G-Compatible IoT Applications

Xiaoqiang Gu, *Graduate Student Member, IEEE*, Srinaga Nikhil N, *Graduate Student Member, IEEE*, Lei Guo, Simon Hemour, *Senior Member, IEEE*, and Ke Wu, *Fellow, IEEE*

***Abstract*— A novel diplexer-based fully passive transponder is presented in this paper, which targets sub-6-GHz 5G-compatible internet-of-things applications. To alleviate the antenna design restrictions of traditional transponder with two separate antennas, a new architecture has been proposed with the introduction of a diplexer, which allows transponder to simply employ a dual-band antenna. In this paper, a dual-band circularly polarized omnidirectional spiral slot antenna, with enhanced bandwidth and gain performance, is designed as the transponder Tx/Rx antenna. Besides the new architecture, a diode selection criterion is proposed as well. Analytical models are derived, showing relationships between the diode's SPICE parameters and the conversion efficiency or conversion loss (CL) of such diode-based transponders. With help of the analysis, transponder designers can easily identify diodes to implement transponders with better performance. Under the guidance of the criterion, low-barrier diode SMS7630 is chosen for verification. Measured CL results of the transponder circuitry part show a noticeable improvement over the state-of-the-art works. The complete prototype was tested with radar's transmitting power of 25 dBm, and it presents a maximum read-out distance up to 7 m when the operating fundamental frequency is 3.5 GHz.**

***Index Terms*— 5G applications, diplexer, frequency doubler, harmonic radar, harmonic tag, harmonic transponder, RFID, Schottky diodes, target detection.**

I. Introduction

THE entire world is about to embrace f fth generation (5G) communication technology by 2020 or so [1]. Recently, a two-hop relay based on an integrated millimeter wave/sub-6-GHz 5G network has been evaluated, featuring a combination of high data rates and a larger coverage [2]. In an early phase of commercialization, the sub-6-GHz frequency band seems a more practical choice in terms of reusing all the existing base stations and design expertise/practices. Specif cally, the lower part of C band (3.4–3.6 GHz) has been allocated as a new IMT band at World Radiocommunication Conference 2015 (WRC-15), making this frequency band a hot topic among the 5G community [3]–[6]. Also, with a rapid development, the internet-of-things (IoT) technology is no more simply a buzzword of today. The number of IoT devices is forecast to reach approximately 28 billion by 2021 [7]. Meanwhile, 5G and IoT technologies are not advancing in parallel separately. For example, 5G speeds up expanding and maturity of IoT technology [8]. Thus, 5G-compatible IoT technology is believed to be a new trend, offering new business opportunities for global economic growth and shaping our future life [9].

Wireless sensing, as one of the main applications in the scope of 5G-compatible IoT applications, becomes an ever-challenging task, due to an increasing number of sensor nodes and a combination of heterogeneous networks. Sensing system with desirable features, such as high reliability, low cost, compact size, and ultralow power consumption, is highly demanded. Harmonic radar and transponder-based sensing system is an attractive candidate to resolve such dilemmas. This technology was explored more than 50 years ago and has gone through a fast development since then [10]. In this concept, the radar interrogates a transponder at the fundamental frequency f_0. The transponder attached on the target then ref ects a higher harmonic, which can be detected by the radar system. Such transponders are realized at the second-harmonic frequency $2f_0$ in most cases [11]. Due to its high robustness to radar clutter interference, harmonic radar and transponder-based sensing system has already been applied in many different scenarios, such as studying bumble bee's foraging range [12], tracking wood frogs [13], RECCO avalanche victim searching system [14], and cracked wall monitoring [15].

For the transponder design, a traditional topology consists of a pair of antennas (one for receiving and the other for transmitting) and a nonlinear device, as shown in Fig. 1. For the resonant antennas, since the Rx antenna operating at the fundamental frequency f_0 would resonate at the second-harmonic frequency $2f_0$, high isolation between Tx and Rx antennas is highly desired to obtain a good performance.

Manuscript received September 4, 2018; revised October 19, 2018; accepted October 24, 2018. This work was supported by the Natural Sciences and Engineering Research Council of Canada. This paper is an expanded version from the IEEE MTT-S Wireless Power Transfer Conference, Montreal, QC, Canada, June 3–7, 2018. *(Corresponding author: Lei Guo.)*

X. Gu, S. N. N, L. Guo, and K. Wu are with the Poly-Grames Research Center, Department of Electrical Engineering, École Polytechnique de Montréal, Montreal, QC H3T 1J4, Canada (e-mail: xiaoqiang.gu@polymtl.ca; lei.guo@polymtl.ca).

S. Hemour is with CNRS, University of Bordeaux, 33 045 Talence, France, and also with the IMS Research Center, Department of Science and Technology, University of Bordeaux, 33 045 Talence, France (e-mail: simon.hemour@u-bordeaux.fr).

Color versions of one or more of the f gures in this paper are available online at http://ieeexplore.ieee.org.

Digital Object Identifie 10.1109/TMTT.2018.2883979

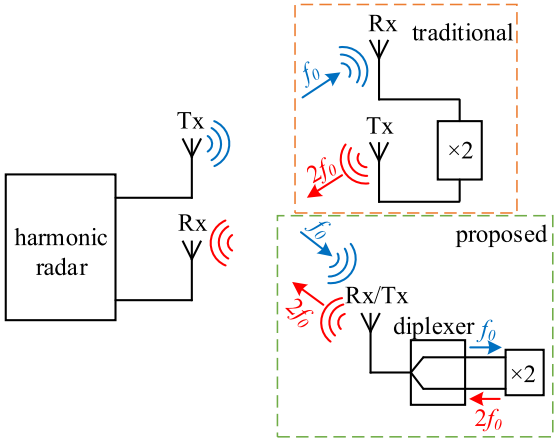

Fig. 1. Architectural comparison of harmonic radar and transponder system based on traditional and proposed topologies.

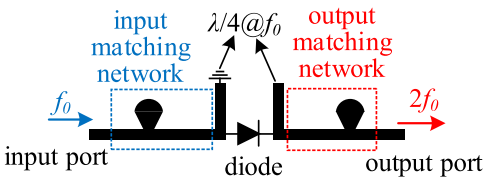

Fig. 2. Circuit schematic of a typical harmonic transponder (second harmonic generation).

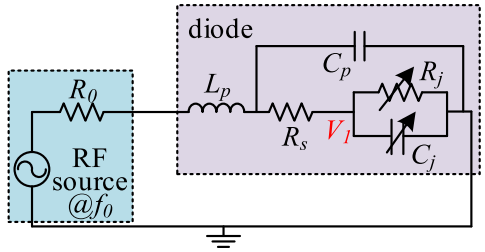

(a)

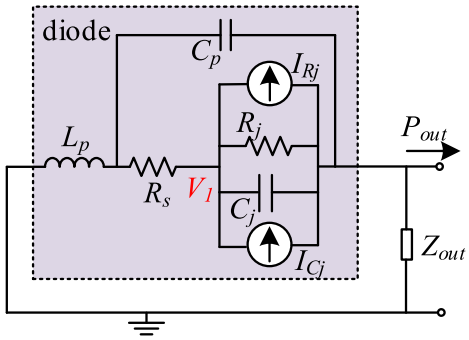

(b)

Fig. 3. Equivalent circuits describe the harmonic transponder operating at different frequencies at the (a) fundamental frequency f_0 and (b) second-harmonic frequency $2f_0$.

For example, to realize such high isolation, linearly polarized antennas have to be placed orthogonally [16]. However, any specific requirement restricts the freedom of the antenna design.

In the scope of this paper, a novel diplexer-based fully passive harmonic transponder is proposed with its topology presented in Fig. 1, along with the conventional architecture for comparison. The diplexer to be introduced in the work has pass-bands for both fundamental and second-harmonic frequencies and provides significant isolation between them. This feature relaxes the antennas design with stringent requirements. Thus, the traditional pair of Tx and Rx antennas designed to have a large isolation at the expense of radiation performance can be simplified as a dual-band antenna optimized for improving its radiation performance and bandwidth.

The initial circuit design and preliminary measurement results were demonstrated in [17]. In this paper, analytical models are proposed to establish relationships between the diode's SPICE parameters and transponder conversion loss (CL). Thus, a diode selection criterion is created, which transponder designers can greatly benefit from. Also, the analysis shows the roles of capacitive and resistive nonlinearity in producing second-harmonic power. To implement a complete transponder, a dual-band circularly polarized spiral slot antenna is designed and fabricated to operate as the transponder antenna. Finally, a joint measurement including the harmonic radar and the complete transponder is performed and the results are analyzed carefully. The integrated fully passive transponder demonstrates an improved CL performance and a noticeable read-out distance of 7 m at the fundamental frequency of 3.5 GHz.

This paper is organized as follows. Section II presents the proposed analytical models of the diode-based harmonic transponder to establish a diode selection criterion. Section III covers design details of the transponder, including separate diplexer, spiral slot antenna designs, and their integration. In Section IV, results from measurements are presented and discussed. Finally, the conclusion is drawn in Section V.

II. Analytical Models of the Harmonic Transponder

The schematic of a typical harmonic transponder circuitry part utilizing second-harmonic generation is presented in Fig. 2. To exacerbate the nonlinear conversion process in the diode, quarter-wave short-circuited and open-circuited stubs are placed around the diode. At the fundamental frequency f_0, the quarter-wave short-circuited stub operates as open at its input, whereas the quarter-wave open-circuited stub evolves into a short end at its input. Thus, the injected RF signal at f_0 passes through the input matching network and reaches out to the diode input. However, the quarter-wave open-circuited stub at f_0 at the output shorts the fundamental signal. The equivalent circuit of the harmonic transponder at the fundamental frequency f_0 can be described as in Fig. 3(a). At the second-harmonic frequency $2f_0$, the short-circuited and open-circuited stubs turn out to be short and open ends, respectively. The diode becomes a second-harmonic energy generator in this case. Due to the stubs and the output matching circuit designed for $2f_0$, maximum second-harmonic power is

sensed at the output port. The equivalent circuit depicting the above scenario is presented in Fig. 3(b).

Note that the input and output matching networks are removed for simplification. The diode is represented by the Shockley model, consisting of junction resistance R_j, junction capacitance C_j, and series resistance R_s [18]. Parasitic capacitance C_p and inductance L_p are used to model the packaging effect. The fundamental RF source is described by a Thevenin equivalent circuit in Fig. 3(a), whereas the diode serving as a second-harmonic source is modeled by a Norton equivalent circuit in Fig. 3(b). Also, V_1 is the node voltage as shown in Fig. 3.

A. Explicit Model A

The injecting fundamental RF signal is assumed to have a cosine waveform with a magnitude of V_0 and angular frequency of ω_0. Therefore, it can be expressed as

$$V_{\text{in}} = V_0 \cos(\omega_0 t). \tag{1}$$

As shown in Fig. 3(a), the voltage across the diode junction can be expressed by

$$V_{\text{ON}} = V_1 \cos(\omega_0 t). \tag{2}$$

The exponential model of describing diode's current I and voltage V is adopted here [19]

$$I_{\text{diode}} = I_s \times \left[e^{\frac{V_{\text{ON}}}{n \times Vt}} - 1\right] = I_s \times \left[e^{\frac{V_1 \cos(\omega_0 t)}{n \times Vt}} - 1\right] \tag{3}$$

where I_s is diode's saturation current and n is the ideality factor. $V_t = k \times T/q$ represents the thermal voltage. k, T, and q are Boltzmann's constant, operating temperature (in Kelvin), and electron charge, respectively. This exponential IV model remains valid in the analysis since the power dealt with by the harmonic transponder is usually small. By using small signal theory, the IV model can be expanded by the Taylor series around the 0 V bias point [20], [21]

$$I_{\text{diode}} = I_s \times \left[\frac{V_{\text{ON}}}{n \times Vt} + \frac{V_{\text{ON}}^2}{(n \times Vt)^2 2!} + \cdots + \frac{V_{\text{ON}}^n}{(n \times Vt)^n n!} + \cdots\right]. \tag{4}$$

The first two terms can be used for approximation in a low power range. Thus, substituting (2) into (4), one can obtain the fundamental current and then calculate the absorbed fundamental power level

$$P_{f0\_\text{A}} = \frac{I_s \times V_1^2}{2 \times n \times Vt}. \tag{5}$$

As can be seen from Fig. 3(b), at the second-harmonic frequency $2f_0$, the junction can be considered as a power generator. The second-harmonic current due to the junction resistance can also be extracted based on (4)

$$I_{Rj} = \frac{I_s \times V_1^2}{4 \times (n \times Vt)^2} \times \cos(2\omega_0 t). \tag{6}$$

The voltage-controlled junction capacitance is characterized by

$$C_j(V_{\text{ON}}) = C_{j0} \times \left(1 - \frac{V_{\text{ON}}}{V_j}\right)^{-M} \tag{7}$$

where V_j and M are junction potential and grading coefficient, respectively. C_{j0} is the zero bias junction capacitance. Note that the diffusion capacitance is not considered in the analysis when the diode is forward biased. Thus, the charge stored in the junction capacitance is

$$Q_{Cj}(V_{\text{ON}}) = \int C_j(V_{\text{ON}}) dV_{\text{ON}} = \frac{C_{j0} \times V_j}{M-1} \times \left(1 - \frac{V_{\text{ON}}}{V_j}\right)^{1-M}. \tag{8}$$

By applying Taylor series to Q_{Cj} and getting the second term as an approximation, the current becomes

$$I_{Cj} = \frac{d\{Q_{Cj}(V_{\text{ON}})\}}{dt} \approx \frac{d\left\{\frac{C_{j0} \times M}{2V_j} \times V_{\text{ON}}^2\right\}}{dt}. \tag{9}$$

I_{Cj} is obtained by substituting (2) into (9)

$$I_{Cj} \approx -\frac{C_{j0} \times M \times V_1^2 \times \omega_0}{2V_j} \times \sin(2\omega_0 t). \tag{10}$$

It can be observed that I_{Rj} and I_{Cj} have a phase difference of 90°. Then, the total current at the second-harmonic frequency $2f_0$ can be written as

$$I_t = \frac{I_s \times V_1^2}{4 \times (n \times Vt)^2} - i \times \frac{C_{j0} \times M \times V_1^2 \times \omega_0}{2V_j}. \tag{11}$$

Note that I_t is the short-circuited current of the diode source. Before calculating the output current I_{out} through applying the current division rule, the source internal impedance Z_p of the diode needs to be determined first

$$Z_p = \frac{R_{j0} \times (i2\omega_0 C_{j0})^{-1}}{R_{j0} + (i2\omega_0 C_{j0})^{-1}} \tag{12}$$

in which $R_{j0} = nV_t/I_s$ is the zero bias junction resistance. Then I_{out} is obtained by

$$I_{\text{out}} = I_t \times \frac{Z_p}{Z_p + R_s + Z_{\text{out}}}. \tag{13}$$

The packaging capacitance and inductance are not included for simplification in this model. Then, the total generated second-harmonic power can be expressed as

$$P_{2f0\_\text{A}} = \text{real}\left(\frac{I_{\text{out}}^* \times I_{\text{out}} \times (Z_p + R_s + Z_{\text{out}})}{2}\right). \tag{14}$$

Thus, the conversion efficiency from fundamental frequency to second-harmonic frequency can be defined as

$$\eta = \frac{P_{2f0\_\text{A}}}{P_{f0\_\text{A}}} = \frac{P_{f0\_\text{A}}}{2} \times \left(\frac{\Re_{10}^2}{4} + \frac{(\omega_0 C_{j0} M R_{j0})^2}{V_j^2}\right) \times \text{real}\left(\frac{Z_p^* \times Z_p}{Z_p^* + R_s + Z_{\text{out}}}\right) \tag{15}$$

where $\Re_{I0}$ is zero bias current responsivity and calculated by $1/(2 \times n \times Vt)$. Based on (15), one knows that to increase the conversion efficiency, a higher input power works like the case of a low-power rectifier. $\Re_{I0}$ is usually associated with the inherent nature of junction. Thus, finding a diode with smaller junction potential V_j and series resistance R_s, but larger grading coefficient M can enhance the conversion efficiency.

B. Accurate Model B

Several approximations are made in model A to get an explicit expression (15) clearly showing the relationship between key SPICE parameters and the conversion efficiency. To get a more accurate model, modification in calculating the fundamental input power and the second-harmonic current due to junction resistance R_j are required [22].

The Bessel function can be used to extract each harmonic component of the diode current in (3) effectively [23]. Therefore, the fundamental current can be written as

$$I_{f0} = I_s \times \left[2 \times i \times J_1\left(-i\frac{V_1}{n \times Vt}\right)\right] \times \cos(\omega_0 t) \quad (16)$$

where $J_v(x)$ is the Bessel function of first kind of order v. The injecting current can be obtained by applying the Kirchhoff Circuit Laws considering the effect of the packaging components

$$I_{\text{in}} = I_{f0} + V_1 \times i\omega_0 C_j + ((I_{f0} + V_1 \times i\omega_0 C_j) \times R_s + V_1) \times i\omega_0 C_p. \quad (17)$$

Meanwhile, the injecting voltage can be expressed by

$$V_{\text{in}} = V_1 + (I_{f0} + V_1 \times i\omega_0 C_j) \times R_s + I_{in} \times i\omega_0 L_p. \quad (18)$$

Hence, the injecting power can be calculated by

$$P_{f0\_\text{B}} = \text{real}\left(\frac{V_{in} \times I_{in}^*}{2}\right). \quad (19)$$

In the calculation of P_{f0_B}, C_j is simplified to be zero bias value C_{j0} in the power range of interest. Note that there is only one unknown V_1 in (19). So, when P_{f0_B} is assigned, V_1 can be easily obtained by solving (19). Next, based on (3), I_{Rj_B} can be obtained by selecting the component at the second-harmonic frequency $2f_0$

$$I_{Rj\_B} = I_s \times \left[-2 \times J_2\left(-i\frac{V_1}{n \times Vt}\right)\right] \times \cos(2\omega_0 t). \quad (20)$$

Together with I_{Cj} expressed in (10), the generated second-harmonic current is

$$I_{t\_B} = I_s \times \left[-2 \times J_2\left(-i\frac{V_1}{n \times Vt}\right)\right] - i \times \frac{C_{j0} \times M \times V_1^2 \times \omega_0}{2V_j}. \quad (21)$$

Next, the current coming out of the diode I_{out_B} can be written by

$$I_{\text{out}\_B} = I_{t\_B} \times \frac{Z_p}{Z_p + R_s + \frac{(Z_{\text{out}} + i2\omega_0 L_p) \times (i2\omega_0 C_p)^{-1}}{Z_{\text{out}} + i2\omega_0 L_p + (i2\omega_0 C_p)^{-1}}} \cdot \frac{(i2\omega_0 C_p)^{-1}}{Z_{\text{out}} + i2\omega_0 L_p + (i2\omega_0 C_p)^{-1}} \quad (22)$$

TABLE I
KEY SPICE PARAMETERS

Parameters	SMS7630 -079LF	HSMS-28 50	HMPS-28 20	SMV1430
C_{j0} (pF)	0.14	0.18	0.7	1.11
I_s (A)	5e-6	3e-6	2.2e-8	1e-14
R_s (Ω)	20	25	8	3.15
n	1.05	1.06	1.08	1
V_j (V)	0.34	0.35	0.65	0.86
M	0.4	0.5	0.5	0.5
C_p (pF)	0.16	0.08	0.08	0.13
L_p (nH)	0.7	2	2	0.7

* Diodes SMS7630 and SMV1430 are from Skyworks. Inc. The remaining two are from Avago Technology.
** All diodes are Schottky diodes except a varactor SMV1430.

where Z_{out} is the output impedance equal to the complex conjugate of the packaged diode's impedance in order to maximize the power transfer to the output port. Then, the generated second-harmonic power reaching the output can be expressed by

$$P_{2f0\_\text{B}} = \text{real}\left(\frac{I_{\text{out}\_B}^* \times I_{\text{out\_B}} \times Z_{\text{out}}}{2}\right). \quad (23)$$

Thus, the conversion efficiency can be calculated

$$\eta = \frac{1}{2}[I_{Rj\_B}^2 + I_{Cj}^2] \cdot \text{real}\left(\left|\frac{Z_p}{Z_p + R_s + \frac{(Z_{\text{out}} + i2\omega_0 L_p) \times (i2\omega_0 C_p)^{-1}}{Z_{\text{out}} + i2\omega_0 L_p + (i2\omega_0 C_p)^{-1}}} \times \frac{(i2\omega_0 C_p)^{-1}}{Z_{\text{out}} + i2\omega_0 L_p + (i2\omega_0 C_p)^{-1}}\right|^2 \times Z_{\text{out}}\right). \quad (24)$$

Correspondingly, the CL in dB (a different way expressing the conversion efficiency) then can be easily determined by

$$\text{CL} = P_{f0\_\text{B}}(\text{dBm}) - P_{2f0\_\text{B}}(\text{dBm}). \quad (25)$$

Several commonly used diodes are selected for verifications. Their key SPICE parameters are listed in Table I. Since the calculation starts from the I–V relationship of the selected diode and the input power of the diode is then obtained, the source impedance is not specified in both models. During the verification, the input power is swept from −50 to −30 dBm. Calculated CL results along with simulated results by ADS Harmonic Balance simulator of each diode-based transponder are presented in Fig. 4. It can be clearly observed that the calculated CL results are in good agreement with the simulated ones by ADS, verifying the great accuracy of the proposed analytical model B. Moreover, diode SMS7630 shows a better CL performance than the others in the power range of interest.

Good accuracy of model B can help us study the contributions of capacitive nonlinearity C_j and resistive nonlinearity R_j, in terms of generating the second-harmonic power.

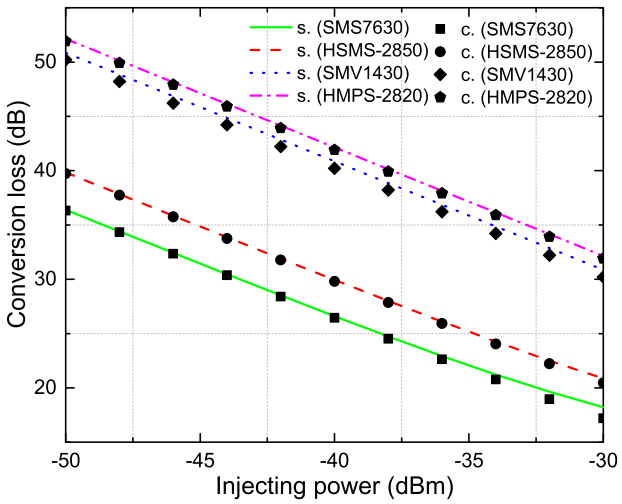

Fig. 4. Comparison of calculated and simulated CL performance of four typical selected diode-based transponders, when the injecting power is in a range of −50 to −30 dBm. The diodes are SMS7630, HSMS-2850, SMV1430, and HMPS-2820.

As can be seen from Fig. 5(a), the CL is calculated based on SMS7630, with all parameters kept the same but C_{j0} swept from 0.1 to 1.2 pF and I_s from 0.01 pA to 10 μA. I_s is inversely proportional to R_{j0}, so the variation of R_{j0} is from 2.7 kΩ to 2.7 TΩ. The corresponding values of R_{j0} have also been listed in Fig. 5(a) and (b). The power level in this analysis is −30 dBm. Four diode candidates are labeled in Fig. 5(a) and (b) based on their C_{j0} and R_{j0} values. Note that it is assumed that SPICE parameters of other diodes are the same as SMS7630 except C_{j0} and R_{j0} in this plotting. This assumption is based on diode's C_{j0} and R_{j0} are two dominant factors determining the CL performance. By doing so, one can easily know the performance of each diode-based transponder. SMS7630 and HSMS-2850 are clearly better choices. Also, Fig. 5(a) and (b) helps to establish a transponder diode selection criterion regarding R_{j0} and C_{j0}, which is higher R_{j0} (lower I_s) and lower C_{j0} are desired. However, considering the potential diff culty of matching network design due to an extremely high R_{j0}, it is almost impossible to use diodes which locate in the left bottom corner of Fig. 5(a). Together with the conclusions based on model A regarding V_j, R_s, and M, a complete diode selection criterion has been successfully established.

Also, the ratio of power due to resistive nonlinearity over total generated second-harmonic power can be calculated by

$$\text{Ratio} = \frac{I_{Rj}^2}{I_{Cj}^2 + I_{Rj}^2}. \tag{26}$$

This ratio is plotted in Fig. 5(b). The red line denotes 50%, which means that C_j and R_j contribute equally to the generation of the second-harmonic power. The location of diode SMS7630 is close to the red line. Also, if a better-performed diode can be found as mentioned before, its capacitive nonlinearity will be dominant in second-harmonic power generation.

Among the four candidates, the best diode SMS7630 is selected to investigate the contributions of C_j and R_j in terms of different power levels. As shown in Fig. 5(c), R_j becomes more dominant with the increase of the injecting power.

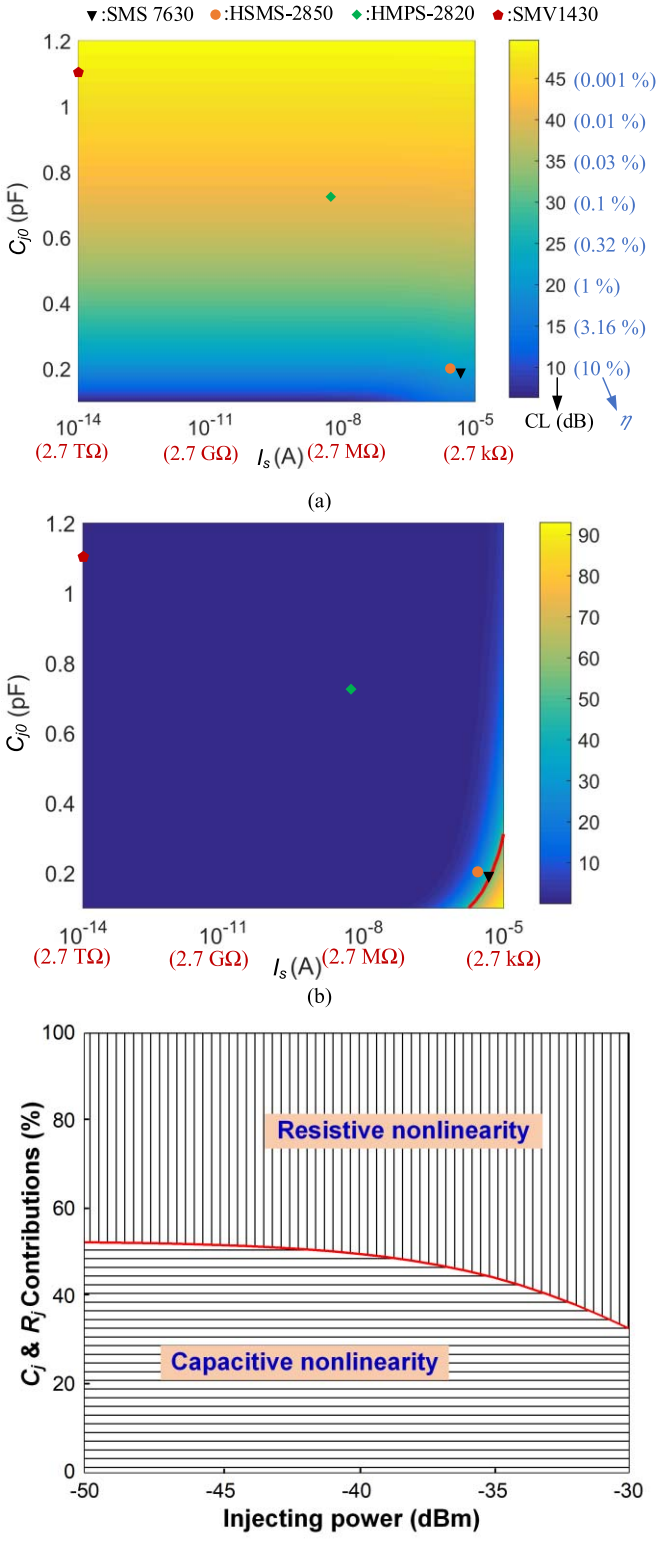

Fig. 5. (a) Calculated CL results when sweeping C_{j0} and I_s (R_{j0}). Four diode candidates are labeled according to their C_{j0} and I_s (R_{j0}). (b) Calculated ratio of power due to resistive nonlinearity over total generated second-harmonic power, when sweeping C_{j0} and I_s (R_{j0}). (c) Contribution of C_j and R_j of diode SMS7630 versus injecting power from −50 to −30 dBm.

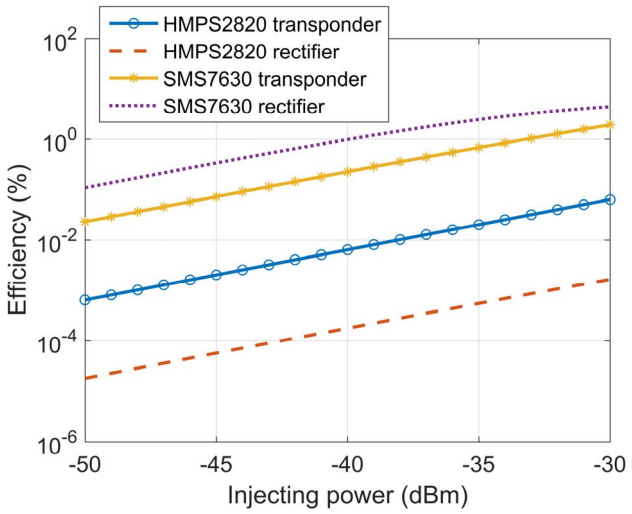

Fig. 6. Efficien y performance comparison of the same diode-based transponder and rectifie . The selected diodes are HMPS2820 and SMS7630.

The nonlinearity of diodes is commonly used in frequency conversion. Another popular application scenario is applying diodes for rectif er design, which converts RF power into dc power. The conversion mechanism is similar. Thus, a comparison of diode's performance in two different application situations could be meaningful. Fig. 6 shows the conversion efficien y performance of two diodes-based rectifier and transponders. SMS7630 behaves better when used in rectif er while HMPS 2820 better for the transponder. According to it, one knows that for a specif c design, a careful selection is essential. Thanks to the criterion addressed in this paper and our previous work regarding rectif er diode analysis, it is hoped that transponder and rectif er design can become more convenient.

III. Integrated Design of the Harmonic Transponder

A. Diplexer Design

As the component offering two passbands and high isolation between ports, the diplexer plays a vital role in this circuitry [24]. The fundamental frequency f_0 of the diplexer is 3.5 GHz according to the new IMT allocated by WRC-15. In this diplexer, port 1 connects to the transponder antenna, through which the fundamental signal is injected into the circuit. Due to the strong coupling between ports 1 and 3, the injected fundamental signal reaches port 3. Subsequently, it goes through the transponder circuitry shown in Fig. 2 and generates second harmonic which reaches port 2. At the second-harmonic frequency $2f_0$, ports 2 and 1 are strong coupled. So, the second harmonic signal reaches port 1 and radiates through the transponder antenna. The smooth signal transmission also relies on a strong suppression of fundamental and second harmonics between ports 2 and 3, respectively.

In the middle of the diplexer circuit, a U-shaped half wavelength open-circuited microstrip line resonator at the fundamental frequency f_0 is inserted, as presented in Fig. 7(a). The locations of each port around the resonator are crucial to

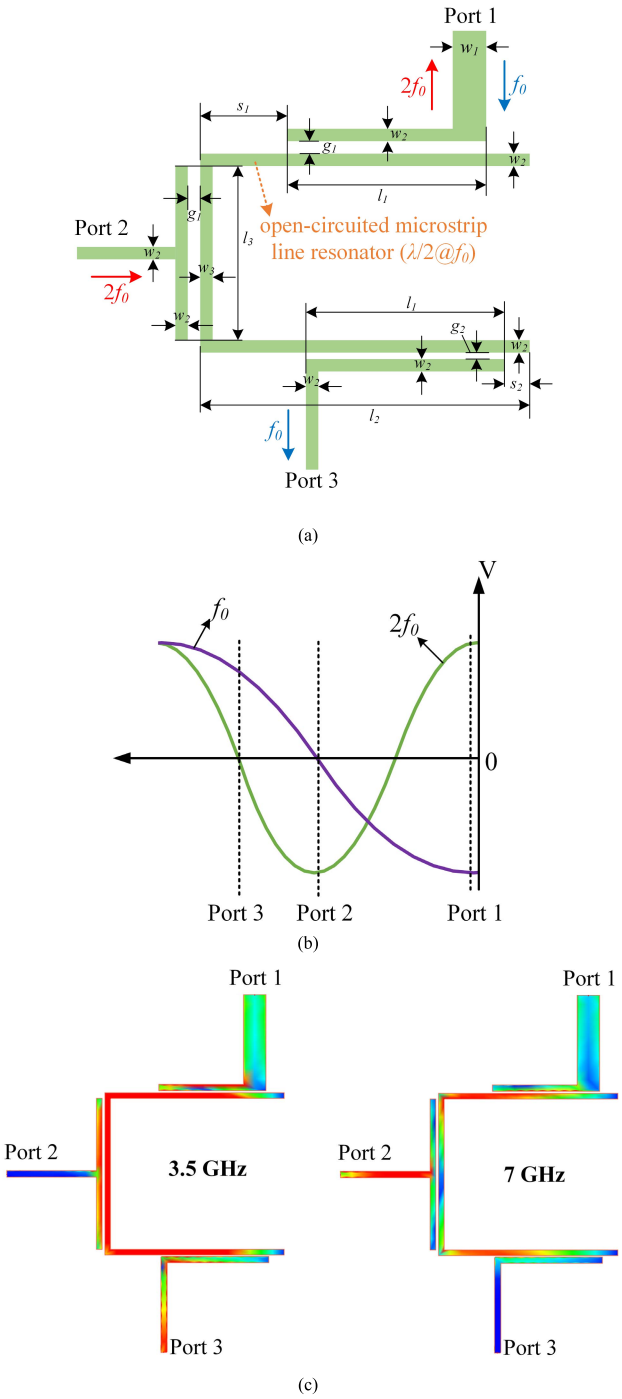

Fig. 7. (a) Layout of the diplexer. Dimensions: $w_1 = 1.27$, $w_2 = 0.323$, $w_3 = 0.34$, $l_1 = 6$, $l_2 = 10$, $l_3 = 8.38$, $g_1 = 0.127$, $g_2 = 0.08$, $s_1 = 3$, $s_2 = 0.86$, in mm. (b) Voltage distribution for an open-circuited microstrip line resonator at the fundamental and second-harmonic frequencies. The locations of each port are labelled along the resonator. (c) Current distributions.

accomplish such a strong coupling and suppression of desired modes simultaneously. Fig. 7(b) illustrates the voltage distribution for an open-circuited microstrip line at the fundamental and second-harmonic frequencies, respectively. At the fundamental frequency f_0, it is obviously better for ports 1 and 3 to be placed at the two ends to obtain a strong coupling. Note that the same microstrip line evolves into a λ resonator at the second-harmonic frequency $2f_0$. To ensure a desired

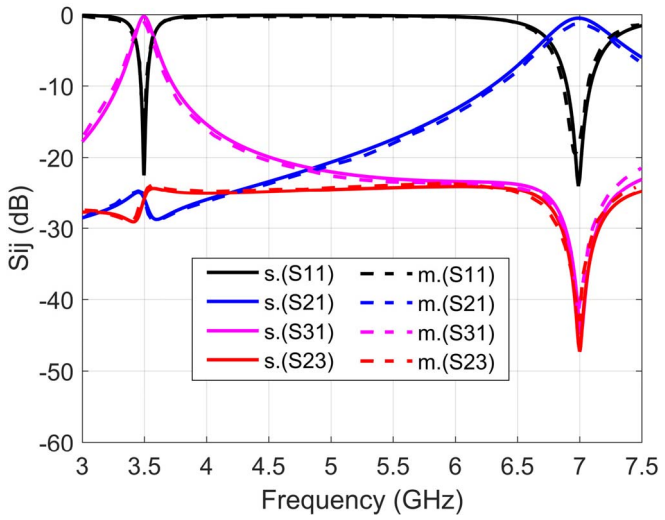

Fig. 8. Comparison of the measured and simulated S-parameters of the diplexer.

strong coupling, port 2 needs to be located in the middle and at the same time port 1 remains at one end. It is observed that during the transmission of the fundamental tone between ports 1 and 3, no power would leak out to port 2. However, port 3 has to be moved to a location where zero voltage occurs on the resonator as shown in Fig. 7(b), in order to minimize the leakage of second-harmonic power to port 3. Such a rough analysis enables quickly locating each port around the resonator. The exact dimensions of the diplexer are obtained through a postoptimization, which are all listed in the caption of Fig. 7. The current distributions at the fundamental and second-harmonic frequencies are demonstrated in Fig. 7(c). The characteristic impedance of microstrip line at port 1 is designed to be 50 Ω, and at ports 2 and 3 to be 100 Ω. The substrate used here is Rogers RT/duroid 6002 with 20-mil thickness and 18-μm copper cladding.

The proposed diplexer is simulated by ADS Momentum microwave simulator. Fig. 8 presents the comparison of simulated and measured S-parameter results, which match well. Although the measurement was conducted using a standard 50-Ω lab setup, the measured results are transformed to a 100-Ω reference for a fair comparison with the simulation results for ports 2 and 3 and presented in Fig. 8. The results shown are the measured insertion loss values of the passbands at the fundamental and second-harmonic frequencies are both less than 1.5 dB, and measured isolation between ports 2 and 3 at both frequencies is over 25 dB.

B. Circuit Integration

With the aid of the aforementioned analytical models and analysis of multiple diodes for CL performance in Section II, the outperforming diode SMS7630-079LF is selected for designing the transponder circuitry. The transponder circuitry integration with the proposed diplexer is presented in Fig. 9(a). The input and output ports shown in Fig. 2 are, respectively, connected with the ports 3 and 2 of the diplexer in Fig. 7(a). The impedance matching between port 3 and the diode is

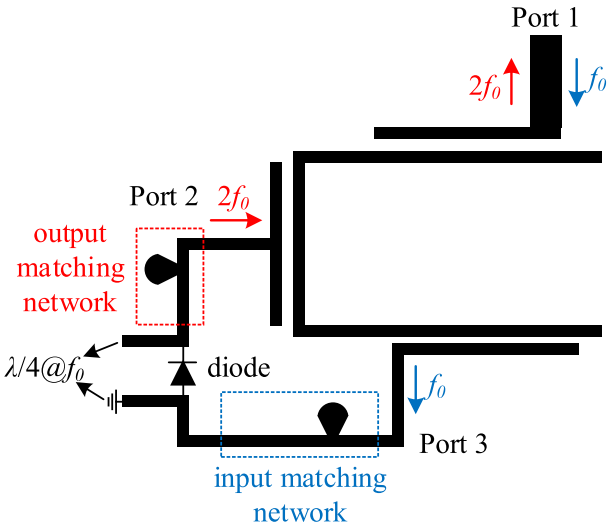

(a)

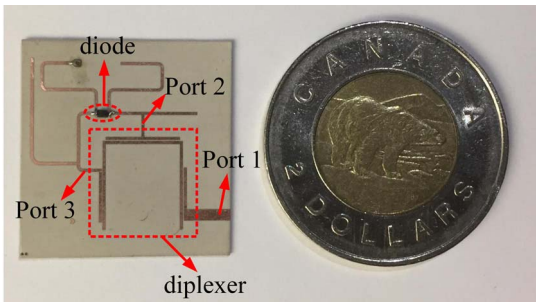

(b)

Fig. 9. (a) Circuit schematic of the diplexer-based harmonic transponder. (b) Experimental prototype.

realized by the input matching network at the fundamental frequency f_0. At the output port, the diode impedance is matched to port 2 by the output matching network at the second-harmonic frequency $2f_0$. The diode impedance is mainly dependent on R_j and C_j as shown in (12). Since the selected diode SMS7630 is a low barrier diode, a simple L-matching network is a satisfactory choice in this case.

In this design, power conversion from the fundamental frequency f_0 to the desired second-harmonic frequency $2f_0$ needs to be maximized. In other words, any other harmonic conversion should be reduced, especially RF-to-dc conversion. Thanks to the gap coupling feature of the diplexer, a conventional capacitor working as the dc block is not necessary at the output port any more. Finally, the fabricated circuity part of the transponder demonstrates a compact and well-rounded design, with the experimental prototype shown in Fig. 9(b).

C. Transponder Antenna Design

The antenna designed to integrate with the harmonic transponder circuitry should satisfy the minimum requirements of the dual-band operation, to receive signal at 3.5 GHz and transmit at 7 GHz. Also, the omnidirectional radiation performance is preferred to increase the spatial coverage [25]. Considering a compact and eff cient module, it is better to

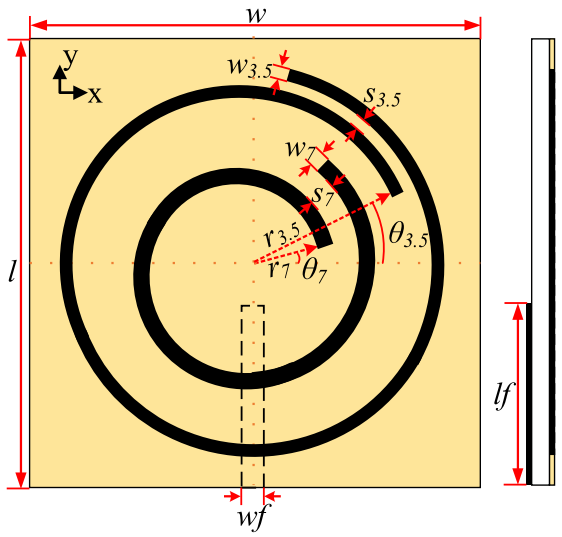

Fig. 10. Top view and side view of proposed dual-band circularly polarized spiral slot antenna with all dimensions marked: $r_{3.5} = 10.3$, $s_{3.5} = 0.57$, $w_{3.5} = 0.95$, $r_7 = 4.8$, $s_7 = 1.6$, $w_7 = 1.3$, $wf = 0.67$, $lf = 13.6$, $w = 35$, and $l = 35$, in mm; $\theta_{3.5} = 20°$, $\theta_7 = 10°$, $N_{3.5} = 1.158$, $N_7 = 1.10$; The substrate is Rogers RT/duroid 6002 of thickness 20 mils, the same one used for the transponder circuitry.

design the antenna utilizing the same ground plane and feed line of the circuitry. Based on these requirements, slot antennas excited by the feed on the other layer of the substrate is an attractive solution. Circular polarization is chosen for the demonstration and is not limited to it. For our application, the dual-band spiral slot antenna proposed in [26] has been improved in bandwidth by replacing the radius variation after each quarter turn with continuous radius variation and aligning the two spiral slots at different angles.

The design is presented in Fig. 10, with all the dimensions marked. It has two spiral slots of different radii to operate as a dual-band antenna at 3.5 and 7 GHz. The spiral on the outer perimeter is designed to operate at 3.5 GHz and the inner one at 7 GHz. These two slots are simultaneously excited through a single microstrip line feed placed on the opposite layer of the substrate. Also, the coupling between these two slots signif cantly improves the bandwidth at both the design frequencies. The spiral slot radius is varied with respect to (27) for both slots

$$r = r_0 + (w + s)N, \quad N = \frac{(\theta - \theta_0)}{2\pi} > 0 \tag{27}$$

where r_0 and θ_0 are the initial radius and initial angle of spiral, w is the width of slot which is constant throughout, s is the spacing between turns, N is the number of turns, and θ is the angle of rotation.

The simulated matching performance of the individual single spiral slots along with that of dual-band spiral slot is presented in Fig. 11(a). The improvement in matching performance of the dual-band spiral slot antenna at both the design frequencies is realized by optimizing the coupling between individual spiral slots. The measured results of the proposed dual-band spiral slot antenna agree well with simulated results for both the matching performance and the axial ratio as shown in Fig. 11(b). It has a measured −10-dB matching

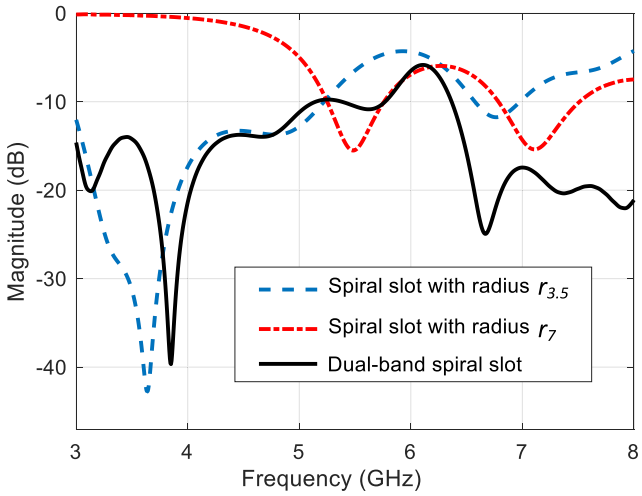

(a)

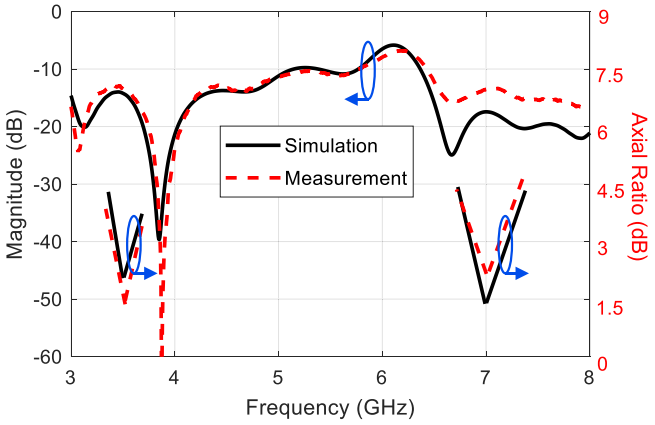

(b)

Fig. 11. Comparison of (a) matching performance for individual spiral slots along with dual-band spiral antenna and (b) simulated and measured matching and axial ratio performance of dual-band spiral slot antenna.

bandwidth of 66% (from 2.9 to 5.8 GHz) at 3.5 GHz and 28% (from 6.3 to 8.4 GHz) at 7 GHz, and a measured axial ratio of 1.56 dB (simulated −2.1 dB) at 3.5 GHz and 2.3 dB (simulated −1.5 dB) at 7 GHz.

E-f eld variation results of the proposed antenna with time at both frequencies are shown in Fig. 12. It shows that the E-fiel varies in a circular pattern, conf rming the circular polarization behavior of the proposed structure at both the design frequencies. It can be observed that the spiral slot with larger radius contributes significa tly for radiation at 3.5 GHz, while the inner spiral slot contributes for 7 GHz.

Radiation eff ciency of the proposed antenna is 98.5% at 3.5 GHz and 98.4% at 7 GHz and has a gain of 4 dB at 3.5 GHz and 3.8 dB at 7 GHz. Simulated radiation pattern for LHCP and RHCP at both the design frequencies are normalized and are shown in Fig. 13. The radiation pattern is measured with the linearly polarized standard gain horn antenna in xz plane and yz plane, at both the frequencies and the normalized results match closely with the simulations, as shown in Fig. 14.

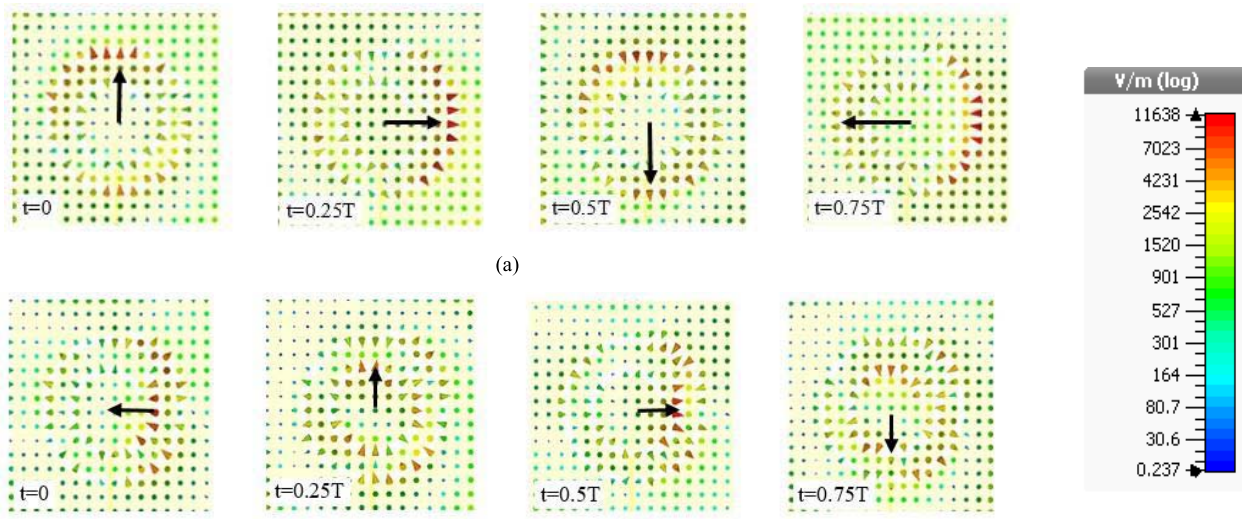

Fig. 12. E-field variation with time at (a) 3.5 and (b) 7 GHz.

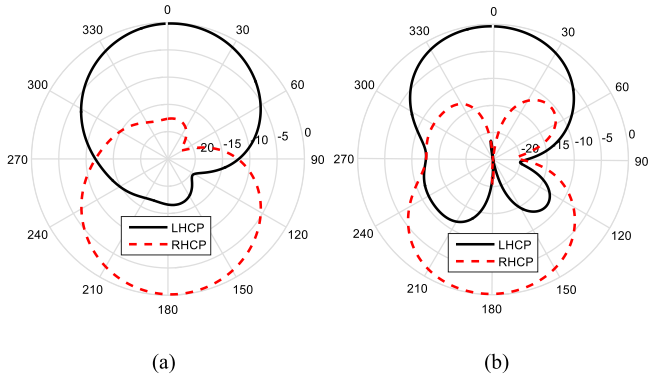

Fig. 13. Simulated LHCP and RHCP at (a) 3.5 and (b) 7 GHz.

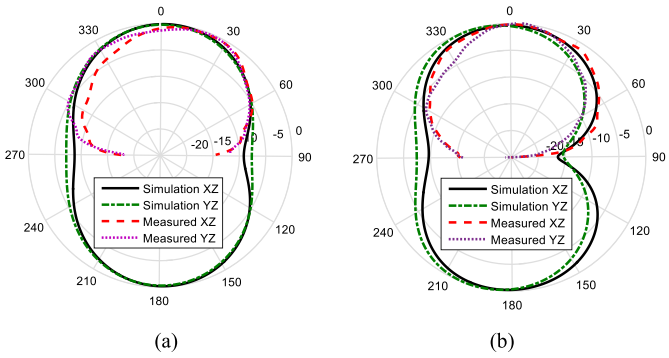

Fig. 14. Comparison of simulated and measured normalized radiation pattern in *xz* and *yz* planes at (a) 3.5 and (b) 7 GHz.

IV. Transponder Measurement and Discussion

As observed from the transponder circuitry in Fig. 9(b), there is only one port (port 1) handling both the receiving and transmitting signals. This necessitates the use of a 3-dB hybrid coupler to detect the output second-harmonic power level in measurements. Fig. 15(a) shows the block diagram of the measurement setup, including the power transfer at two frequencies. The signal generator connected to port A of the hybrid coupler provides power at the fundamental frequency f_0. Half of this power reaches the transponder. Then, the second-harmonic output generated by the transponder at port C is transferred to port B, where a half of the power arrives at the signal analyzer. This signal analyzer displays the generated second-harmonic power level. The setup realized in the Poly-Grames Research Center is shown in Fig. 15(b).

The measured CL results of this transponder are demonstrated in Fig. 16, excluding all insertion loss of the coupler and cables. The input power range in the measurement is from -35 to -25 dBm. The simulated results from ADS Harmonic Balance simulator are included in comparison with measured ones, demonstrating a good match between them. Also, the CL results reported by previous related works are presented for comparison [15], [27]. By careful study and utilizing of identifie low-barrier diode, the CL performance of the proposed fully passive transponder has been improved greatly compared to previous works.

After this preliminary measurement, a joint measurement of the complete transponder is conducted in the lab. From the building block sizes shown in Fig. 17(a), an integrated transponder with dimensions of 60 mm $\times$ 35 mm is feasible. The measurement setup to test the complete transponder is presented in Fig. 17(b). Both the radar Tx/Rx antennas are horn antennas from ETS-Lindgren, which are model 3160-05 and 3160-06. Note that although the frequency range for model 3160-05 is from 3.95 to 5.85 GHz, it still works properly at 3.5 GHz after verifie by S parameters measurements. The radar Tx antenna is connected with a signal generator to radiate fundamental power. And received power by Rx antenna is monitored through a signal analyzer. This describes the setup of the radar side. For the transponder side, the prototype is fixed on a moveable wooden base using tapes as shown in Fig. 17(b).

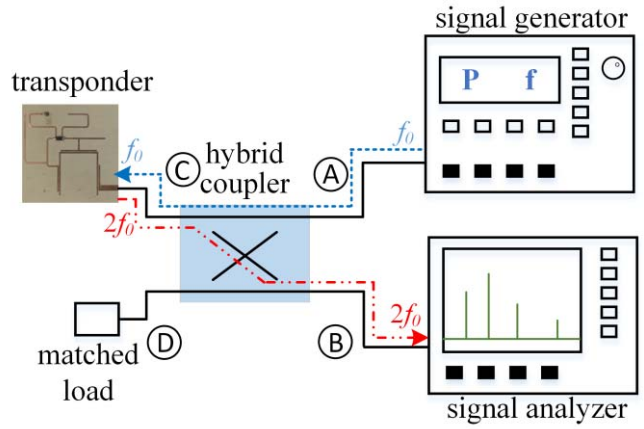

(a)

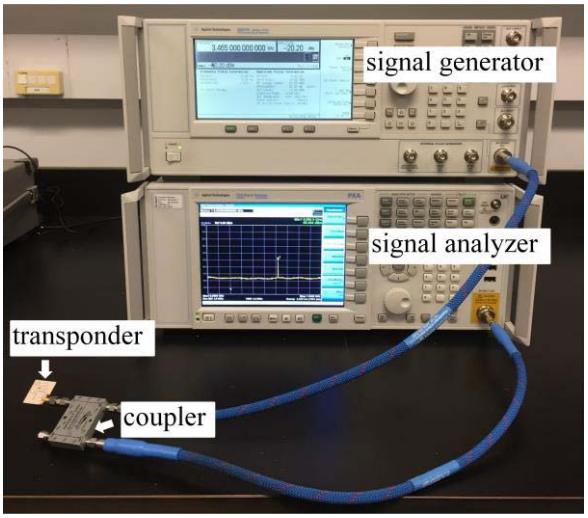

Fig. 15. Measurement setup. (a) Diagram. (b) Realized setup in the laboratory.

Theoretical link budget analysis (in dB) is based on Friis transmission equation [28], which yields

$$P_r = P_t + G_{ra}^t + TL_{f_0} + G_{tr}^r - CL + G_{tr}^t + TL_{2f_0} + G_{ra}^r \quad (28)$$

where the definitions of parameters included are listed below.

The transmission loss is calculated by

$$\mathrm{TL} = 20 \times lg\left(\frac{\lambda}{4\pi d}\right) \quad (29)$$

in which λ is the wavelength and d is the transmission distance.

For measurements, the power level provided by the signal generator is set to be 25 dBm. The gain of the Tx antenna is 16.7 dBi at 3.5 GHz. For the energy detection side, the gain of Rx antenna is 17.1 dBi and the noise floor of the signal analyzer is -100 dBm. The received power by the radar varying distance is presented in Fig. 18. The testing distance starts from 2 m which ensures that both horn antennas are operating in the far-field. In the measurements, the separate antenna and circuit parts are effectively used to obtain the fundamental power illuminating the transponder antenna and

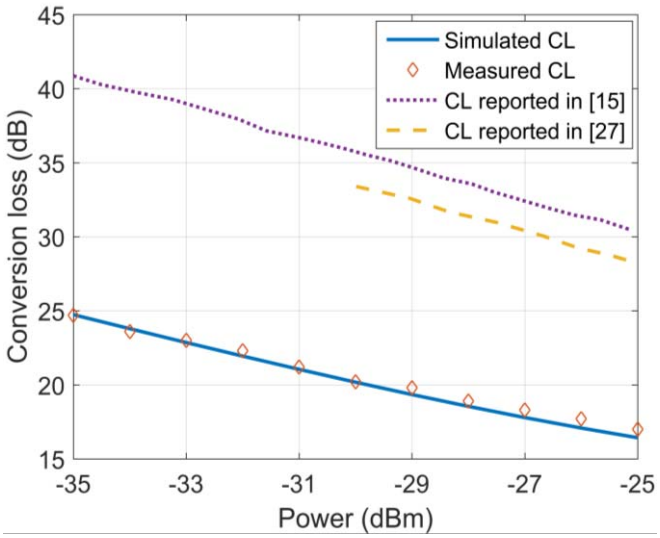

Fig. 16. Comparison of simulated and measured CL results of the proposed harmonic transponder. Some related results reported recently have also been shown for comparison

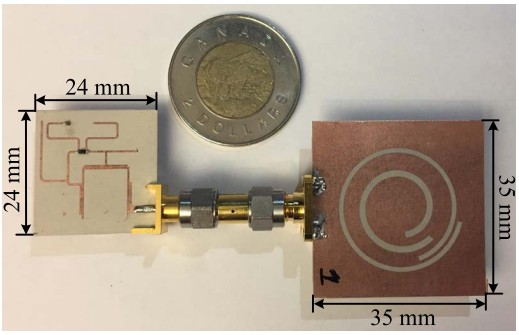

(a)

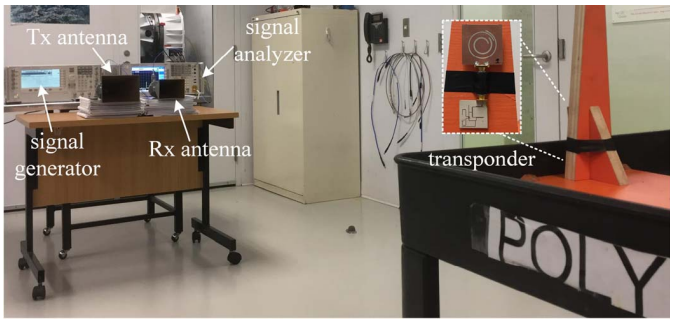

(b)

Fig. 17. (a) Proposed experimental prototype of the transponder. (b) Measurement setup in the laboratory.

the second-harmonic power transmitted by the same transponder antenna. Thus, these data help establish the power link of the harmonic radar and transponder-based system, showing a global picture of each dissipation part. The above information is included in Fig. 18. It clearly shows that the loss due to the transponder is low. Also, in the Fig. 18, calculated received results are also presented for comparison. Considering a noise floor of -100 dBm, the maximum read-out distance for this setup is about 7 m.

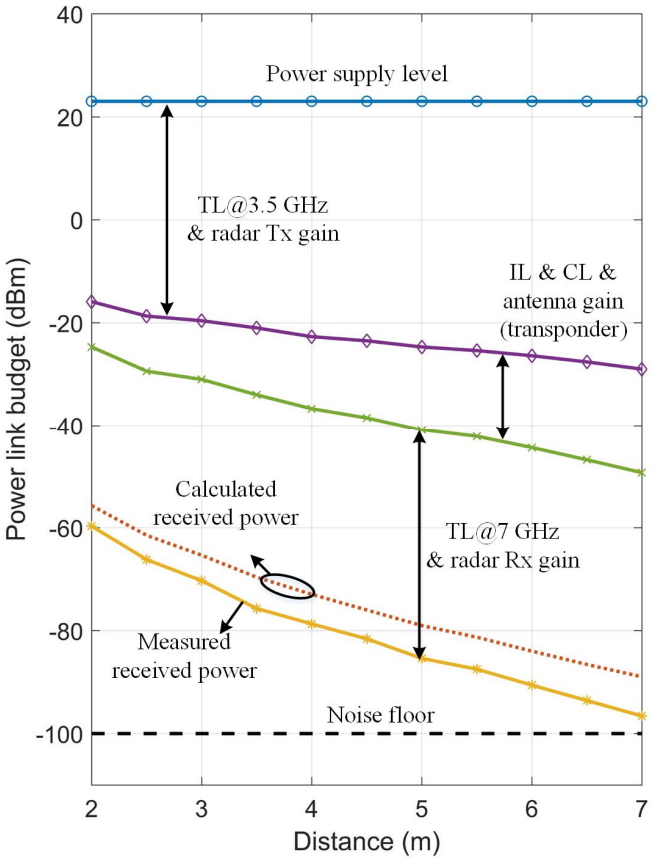

Fig. 18. Calculated power link and measured received power when the proposed transponder is placed in a distance range from 2 to 7 m.

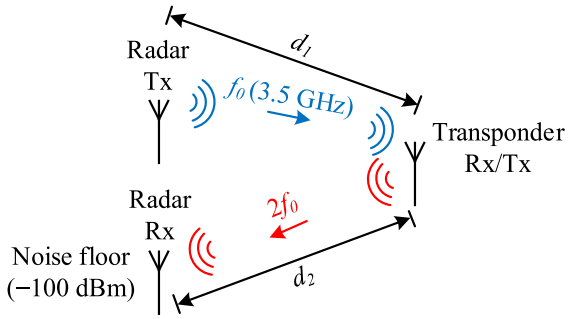

Fig. 19. Setup diagram for the calculation of FOM_d.

To f gure out a fair way to compare our transponder with other state-of-the-art works, the harmonic radar performance and transmission loss due to different frequencies need to be normalized. Thus, it is assumed that each transponder is tested under the same circumstances, which we assume radar transmits 25-dBm power and both Tx/Rx antennas have a gain of 10 dBi. Although each transponder was measured in a different power range within each work, each covers the same injecting power level into diode of −25 dBm. Thus, during the comparison, the diode's injecting power is assumed to be −25 dBm for each transponder. As shown in Fig. 19, the operating fundamental frequency is assumed to be 3.5 GHz. Based on the transponder information provided in each related work, a f gure-of-merit of transponder's maximum

TABLE II

DEFINITIONS OF PARAMETERS IN (28)

Parameters	
P_r	Power received by radar at $2f_0$
P_t	Power transmitted by radar at f_0
G_{ra}^t	Transmitting antenna gain of the radar
TL_{f_0}	Transmission loss in the space at f_0
G_{tr}^r	Receiving antenna gain of the transponder
G_{tr}^t	Transmitting antenna gain of the transponder
TL_{2f_0}	Transmission loss in the space at $2f_0$
G_{ra}^r	Receiving antenna gain of the radar

TABLE III

COMPARISON BETWEEN THIS PAPER AND PREVIOUS RELATED WORKS

work	[15]	[29]	[27]	**this work**
Type	Passive	Passive	Passive	**Passive**
Op. freq. (GHz)	1.2 & 2.4	1 & 2	0.868 & 1.736	**3.5 & 7**
Size (mm^2)	75 × 65	80 × 35	200 × 125	**60 × 35**
No. of ant.	2	1	2	**1**
Ant. Gain (dBi)	3.3@f_0 3@$2f_0$	1.3@f_0 1.7@$2f_0$	1.6@f_0 2.6@$2f_0$	**4@f_0** **3.8@$2f_0$**
Polarization	LP	LP	LP	**CP**
CL (dB) @−25 dBm	26.5	19.9	30	**17**
d_1 / d_2 FOM_d (m)	10.0/4.1 7.0	7.9/7.5 7.7	8.2/2.6 5.4	**10.8/13.3** **12.0**

detection range (FOM_d) can be define and then calculated

$$\text{FOM}_d = \frac{d_1 + d_2}{2} \tag{30}$$

in which

$$d_1 = \frac{c}{f_0 \times 4\pi \times 10^{\frac{-(P_t + G_{ra}^t + 25 + G_{tr}^r)}{20}}} \tag{31a}$$

$$d_2 = \frac{c}{2f_0 \times 4\pi \times 10^{\frac{-(75 - CL + G_{tr}^t + G_{ra}^r)}{20}}}. \tag{31b}$$

Note that the calculation of FOM_d also assumes that the antenna gain and CL of each transponder are still the same at 3.5 GHz.

A comparison between this paper and other state-of-the-art works is listed in Table III. All of them are fully passive harmonic transponders. Our proposed transponder features more freedom of transponder antenna design, thanks to which a dual-band circularly polarized omnidirectional antenna with enhanced bandwidth performance, higher radiation eff ciency, and gain are possible. The proposed transponder is able to deliver lower CL, when the input power level is at −25 dBm. Due to the lower CL and higher transponder antenna gains, our proposed transponder prototype shows a noticeable improvement regarding the FOM_d as shown in Table III. The calculation of FOM_d has several assumptions. For example, all the insertion loss is ignored. The injecting power of transponder

is fi ed to be −25 dBm. Thus, the FOM_d is larger than the measured read-out distance.

V. Conclusion

This paper proposes and presents a novel diplexer-based fully passive transponder. Comparing with traditional architectures with two separate antennas, the proposed transponder allows the antenna design to enjoy more f exibility by adding a diplexer into the circuitry part. Analytical models are proposed to reveal relationships between the diode's SPICE parameters and transponder CL or conversion eff ciency. A selection criterion is established and can be used to simplify the transponder design. With the aid of this criterion, the outperforming low-barrier diode SMS7630-079LF is chosen for experimental ver-if cation. The proposed transponder shows lower CL of 17 dB at the input power of −25 dBm in the measurement, showing a superior performance compared to the state-of-the-art works. A dual-band circularly polarized omnidirectional spiral slot antenna is designed as the transponder Tx/Rx antenna. The antenna shows improved performance regarding gain and bandwidth. In a measurement of the complete transponder, it is able to reach a read-out distance range up to 7 m, when the operating fundamental frequency is 3.5 GHz. This proposed fully passive transponder is believed to have a great potential for sub-6-GHz 5G-compatible IoT applications.

Acknowledgment

The authors would like to thank Dr. F. Zhu for his useful discussions. The authors would also like to thank J. Gauthier, T. Antonescu, M. Thibault, and D. Dousset from the Technical Support Team, Poly-Grames Research Center, Montreal, QC, Canada.

References

[1] W. Fan *et al.*, "A step toward 5G in 2020: Low-cost OTA performance evaluation of massive MIMO base stations," *IEEE Antennas Propag. Mag.*, vol. 59, no. 1, pp. 38–47, Feb. 2017.

[2] J. Deng, O. Tirkkonen, R. Freij-Hollanti, T. Chen, and N. Nikaein, "Resource allocation and interference management for opportunistic relaying in integrated mmWave/sub-6 GHz 5G networks," *IEEE Commun. Mag.*, vol. 55, no. 6, pp. 94–101, Jun. 2017.

[3] WRC-15 Press Release. (Nov. 27, 2015). *World Radiocommunication Conference Allocates Spectrum for Future Innovation*. [Online]. Available: http://www.itu.int/net/pressoff ce/press_releases/2015/56.aspx#.W4Xga2iPKUk

[4] Y. Li, C.-Y.-D. Sim, Y. Luo, and G. Yang, "12-port 5G massive MIMO antenna array in sub-6GHz mobile handset for LTE bands 42/43/46 applications," *IEEE Access*, vol. 6, pp. 344–354, 2017.

[5] Y. Zhu, G. Zheng, L. Wang, K.-K. Wong, and L. Zhao, "Content placement in cache-enabled sub-6 GHz and millimeter-wave multi-antenna dense small cell networks," *IEEE Trans. Wireless Commun.*, vol. 17, no. 5, pp. 2843–2856, May 2018.

[6] H. Elshaer, M. N. Kulkarni, F. Boccardi, J. G. Andrews, and M. Dohler, "Downlink and uplink cell association with traditional macrocells and millimeter wave small cells," *IEEE Trans. Wireless Commun.*, vol. 15, no. 9, pp. 6244–6258, Sep. 2016.

[7] A. Nordrum, "Popular Internet of Things forecast of 50 billion devices by 2020 is outdated," *IEEE Spectr.*, Aug. 16, 2016. [Online]. Available: http://spectrum.ieee.org/tech-talk/telecom/internet/popular-internet-of-things-forecast-of-50-billion-devices-by-2020-isoutdated

[8] L. Lyu, C. Chen, S. Zhu, and X. Guan, "5G enabled codesign of energy-efficien transmission and estimation for industrial IoT systems," *IEEE Trans. Ind. Informat.*, vol. 14, no. 6, pp. 2690–2704, Jun. 2018.

[9] N. Saxena, A. Roy, B. J. R. Sahu, and H. Kim, "Eff cient IoT gateway over 5G wireless: A new design with prototype and implementation results," *IEEE Commun. Mag.*, vol. 55, no. 2, pp. 97–105, Feb. 2017.

[10] J. G. Vogler, D. J. Maquire, and A. E. Steinhauer, "DINADE—A new interrogation, navigation and detection system," *Microw. J.*, vol. 10, no. 6, pp. 2–6, Jun. 1967.

[11] K. Rasilainen, J. Ilvonen, J.-M. Hannula, and V. Viikari, "Designing harmonic transponders using lumped-component matching circuits," *IEEE Antennas Wireless Propag. Lett.*, vol. 16, pp. 246–249, 2017.

[12] J. L. Osborne *et al.*, "A landscape-scale study of bumble bee foraging range and constancy, using harmonic radar," *J. Appl. Ecol.*, vol. 36, pp. 519–533, Sep. 1999.

[13] H. M. Aumann and N. W. Emanetoglu, "A wideband harmonic radar for tracking small wood frogs," in *Proc. IEEE Radar Conf.*, Cincinnati, OH, USA, May 2014, pp. 108–111.

[14] C. Van Tilburg *et al.*, "Wilderness Medical Society practice guidelines for prevention and management of avalanche and nonavalanche snow burial accidents," *Wilderness Environ. Med.*, vol. 28, no. 1, pp. 23–42, Mar. 2017.

[15] V. Palazzi, F. Alimenti, P. Mezzanotte, G. Orecchini, and L. Roselli, "Zero-power, long-range, ultra low-cost harmonic wireless sensors for massively distributed monitoring of cracked walls," in *IEEE MTT-S Int. Microw. Symp. Dig.*, Honolulu, HI, USA, Jun. 2017, pp. 1335–1338.

[16] V. Palazzi, F. Alimenti, C. Kalialakis, P. Mezzanotte, A. Georgiadis, and L. Roselli, "Highly integrable paper-based harmonic transponder for low-power and long-range IoT applications," *IEEE Antennas Wireless Propag. Lett.*, vol. 16, pp. 3196–3199, 2017.

[17] X. Gu, L. Guo, S. Hemour, and K. Wu, "Novel diplexer-based harmonic transponder for 5G-compatible IoT applications," in *Proc. IEEE MTT-S Wireless Power Transf. Conf.*, Montreal, QC, Canada, Jun. 2018, pp. 1–4.

[18] W. Shockley, "The theory of p-n junctions in semiconductors and p-n junction transistors," *Bell Syst. Tech. J.*, vol. 28, no. 3, pp. 435–489, Jul. 1949.

[19] X. Gu, S. Hemour, L. Guo, and K. Wu, "Integrated cooperative ambient power harvester collecting ubiquitous radio frequency and kinetic energy," *IEEE Trans. Microw. Theory Techn.*, vol. 66, no. 9, pp. 4178–4190, Sep. 2018.

[20] S. Hemour and K. Wu, "Radio-frequency rectif er for electromagnetic energy harvesting: Development path and future outlook," *Proc. IEEE*, vol. 102, no. 11, pp. 1667–1691, Nov. 2014.

[21] C. H. P. Lorenz, S. Hemour, W. Liu, A. Badel, F. Formosa, and K. Wu, "Hybrid power harvesting for increased power conversion eff ciency," *IEEE Microw. Wireless Compon. Lett.*, vol. 25, no. 10, pp. 687–689, Oct. 2015.

[22] X. Gu, L. Guo, S. Hemour, and K. Wu, "Analysis and exploitation of diplexer-based fully passive harmonic transponder for 5G applications," in *Proc. IEEE MTT-S Int. Microw. Workshop Ser. 5G Hardw. Syst. Technol.*, Dublin, Ireland, Aug. 2018, pp. 1–3.

[23] G. De Vita and G. Iannaccone, "Design criteria for the RF section of UHF and microwave passive RFID transponders," *IEEE Trans. Microw. Theory Techn.*, vol. 53, no. 9, pp. 2978–2990, Sep. 2005.

[24] K. Wang, A. Ghiotto, and K. Wu, "Harmonic feedback-loop oscillator for pulling effect reduction and improved phase noise," in *IEEE MTT-S Int. Microw. Symp. Dig.*, Tampa, FL, USA, Jun. 2014, pp. 1–4.

[25] E. Vandelle *et al.*, "High gain isotropic rectenna," in *IEEE MTT-S Int. Microw. Symp. Dig.*, Taipei, Taiwan, May 2017, pp. 1–3.

[26] X. L. Bao and M. J. Ammann, "Monofila spiral slot antenna for dual-frequency dual-sense circular polarization," *IEEE Trans. Antennas Propag.*, vol. 59, no. 8, pp. 3061–3065, Aug. 2011.

[27] A. Lazaro, R. Villarino, and D. Girbau, "A passive harmonic tag for humidity sensing," *Int. J. Antennas Propag.*, vol. 2014, Jul. 2014, Art. no. 670345.

[28] H. T. Friis, "A note on a simple transmission formula," *Proc. IRE*, vol. 34, no. 5, pp. 254–256, May 1946.

[29] K. Rasilainen, J. Ilvonen, A. Lehtovuori, J.-M. Hannula, and V. Viikari, "On design and evaluation of harmonic transponders," *IEEE Trans. Antennas Propag.*, vol. 63, no. 1, pp. 15–23, Jan. 2015.

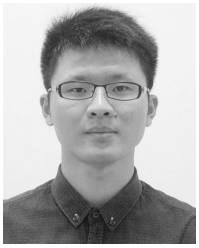

Xiaoqiang Gu (GS'17) was born in Changzhou, China, in 1990. He received the B.Eng. degree from the University of Electronic Science and Technology of China, Chengdu, China, in 2012, and the M.Eng. degree from Zhejiang University, Hangzhou, China, in 2015. He is currently pursuing the Ph.D. degree at the École Polytechnique de Montréal, Montreal, QC, Canada.

His current research interests include wireless power harvesting, multisource energy harvesting, and nonlinear circuit analysis and design.

Mr. Gu was a recipient of the Best Student Paper Award of the 2017 IEEE MTT-S Wireless Power Transfer Conference, Taipei, Taiwan, and the Travel Grant Award of the 2018 IEEE MTT-S International Microwave Workshop Series on 5G Hardware and System Technologies, Dublin, Ireland. He was also among the Best Student Paper f nalists of the 2018 IEEE MTT-S Wireless Power Transfer Conference, Montreal, QC, Canada.

Srinaga Nikhil N (GS'17) was born in Warangal, India, in 1988. He received the M.Tech. degree from the Dhirubhai Ambani Institute of Information and Communication Technology (DA-IICT), Gandhinagar, India, in 2012. He is currently pursuing the Ph.D. degree at the Department of Electrical Engineering, École Polytechnique de Montréal, Montreal, QC, Canada.

He was an Assistant professor with the Marwadi Education Group of Institutions, Rajkot, India, from 2012 to 2014. From 2014 to 2015, he was a Project Assistant with the Indian Institute of Science, Bangalore, India, where he focused on the design of antennas for various industrial applications. His current research interests include unifi d integration of circuits and antennas, active array antennas with beam scanning and beam forming capabilities, and also passive antennas.

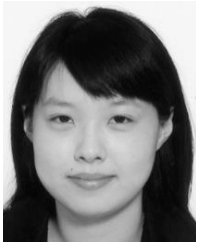

Lei Guo received the B.Eng. degree in communication engineering from the Harbin Institute of Technology, Harbin, China, in 2011, and the Ph.D. degree in electronic engineering from the City University of Hong Kong, Hong Kong, in 2016.

She is currently a Post-Doctoral Research Fellow with the Poly-Grames Research Center, École Polytechnique de Montréal, Montreal, QC, Canada. Her current research interests include dielectric resonator antenna, antenna in package, and energy harvesting.

Dr. Guo was a recipient of the 2015 iWEM Student Best Paper Award.

Simon Hemour (S'08–M'11–SM'16) received the B.S. degree in electrical engineering from the University of Grenoble, Grenoble, France, in 2004, and the M.S. and Ph.D. degrees in optics, optoelectronics, and microwave engineering from the Grenoble Institute of Technology, Grenoble, France, in 2006 and 2010, respectively.

From 2006 to 2007, he was a Research Assistant with the Pidstryhach Institute of Applied Problems of Mechanics and Mathematics, National Academy of Science of Ukraine, Lviv, Ukraine. In 2003, he joined the European Organization for Nuclear Research, Geneva, Switzerland, as a member of the Instrumentation Department, where he was involved with ATLAS experiment on the large Hadron collider. In 2007, he joined the IMEP-LAHC MINATEC Laboratory, Grenoble. From 2011 to 2015, he was with the Poly-Grames Research Center, École Polytechnique de Montréal, Montreal, QC, Canada, where he was leading the Wireless Power Transmission and Harvesting Research Group. He joined the Universite de Bordeaux, Bordeaux, France, in 2015, where he is currently an Associate Professor, and he leads research in wireless microenergy solutions for IoT and biomedical applications. His current research interests include wireless power transfer and hybrid energy harvesting, nonlinear devices, innovative RF measurements, RF interferometry, low-power microwave, and millimeter-wave conversion circuits.

Dr. Hemour is a member of the IEEE MTT-26 Wireless Energy Transfer and Conversion Technical Committee.

Ke Wu (M'87–SM'92–F'01) received the B.Sc. degree (Hons.) in radio engineering from Southeast University, Nanjing, China, in 1982, the D.E.A. degree (Hons.) in optics, optoelectronics, and microwave engineering from the Institut National Polytechnique de Grenoble, Grenoble, France, in 1984, and the Ph.D. degree (Hons.) in optics, optoelectronics, and microwave engineering from the University of Grenoble, Grenoble, France, in 1987.

He was the Founding Director of the Center for Radiofrequency Electronics Research of Quebec (Regroupement Stratgique of FRQNT), Montreal, QC, Canada. He has held guest, visiting, and honorary professorships with many universities around the world. He is currently a Professor of electrical engineering, the Tier-I Canada Research Chair of RF and millimeter-wave engineering, and the NSERC-Huawei Industrial Research Chair of future wireless technologies with the École Polytechnique de Montréal, Montreal, where he has been the Director with the Poly-Grames Research Center. He has authored or co-authored over 1000 refereed papers and a number of books/book chapters. He holds over 30 patents. His current research interests include substrate integrated circuits, antenna arrays, advanced computer aided design and modeling techniques, nonlinear wireless technologies, wireless power transmission and harvesting, development of RF and millimeter-wave transceivers and sensors for wireless systems and biomedical applications, and the modeling and design of microwave and terahertz photonic circuits and systems.

Dr. Wu is a Fellow of the Canadian Academy of Engineering and the Royal Society of Canada (The Canadian Academy of the Sciences and Humanities). He is a member of the Electromagnetics Academy, Sigma Xi, and URSI. He was a recipient of many awards and prizes, including the fir t IEEE Microwave Theory and Techniques (IEEE MTT-S) Outstanding Young Engineer Award, the 2004 Fessenden Medal of the IEEE Canada, the 2009 Thomas W. Eadie Medal of the Royal Society of Canada, the Queen Elizabeth II Diamond Jubilee Medal in 2013, the 2013 FCCP Education Foundation Award of Merit, the 2014 IEEE MTT-S Microwave Application Award, the 2014 Marie-Victorin Prize (Prix du Quebec the highest distinction of Quebec in the natural sciences and engineering), the 2015 Prix dExcellence en Recherche et Innovation of Polytechnique Montreal, and the 2015 IEEE Montreal Section Gold Medal of Achievement. He was an IEEE MTT-S Distinguished Microwave Lecturer from 2009 to 2011. He is the IEEE MTT-S President. He is the Inaugural Three-Year Representative of North America as a member of the European Microwave Association General Assembly. He was an elected IEEE MTT-S Administrative Committee (AdCom) member from 2006 to 2015. He has served as the Chair of the IEEE MTT-S Transnational Committee, the IEEE Member and Geographic Activities Committee, and the Technical Coordinating Committee among many other AdCom functions. He has held key positions in and has served on various panels and international committees, including the Chair of Technical Program Committees, International Steering Committees, and international conferences/symposia. In particular, he was the General Chair of the 2012 IEEE MTT-S International Microwave Symposium. He was the Chair of the joint IEEE Chapters of MTT-S/AP-S/LEOS, Montreal, QC, Canada. He is the Chair of the newly restructured IEEE MTT-S Montreal Chapter. He has served on the Editorial/Review Boards of many technical journals, transactions, proceedings, and letters, and also scientifi encyclopedia, including as an Editor or a Guest Editor.